JACS
JOURNAL OF THE AMERICAN CHEMICAL SOCIETY
Article
Cite This: J. Am. Chem. Soc. 2019, 141, 451−462
pubs.acs.org/JACS

Endogenous Dynamic Nuclear Polarization for Natural Abundance ^{17}O and Lithium NMR in the Bulk of Inorganic Solids

Tamar Wolf,[†] Sandeep Kumar,[‡] Harishchandra Singh,[§] Tanmoy Chakrabarty,[†] Fabien Aussenac,[∥] Anatoly I. Frenkel,[§,@] Dan Thomas Major,[‡] and Michal Leskes*[,†]

[†]Department of Materials and Interfaces, Weizmann Institute of Science, Rehovot 76100, Israel
[‡]Department of Chemistry, Bar-Ilan University, Ramat Gan 52900, Israel
[§]Department of Materials Science and Chemical Engineering, Stony Brook University, Stony Brook, New York 11794, United States
[∥]Bruker BioSpin, 34 rue de l'Industrie BP 10002, 67166 Wissembourg Cedex, France
[@]Division of Chemistry, Brookhaven National Laboratory, Upton, New York 11973, United States

Supporting Information

ABSTRACT: In recent years magic angle spinning-dynamic nuclear polarization (MAS-DNP) has developed as an excellent approach for boosting the sensitivity of solid-state NMR (ssNMR) spectroscopy, thereby enabling the characterization of challenging systems in biology and chemistry. Most commonly, MAS-DNP is based on the use of nitroxide biradicals as polarizing agents. In materials science, since the use of nitroxides often limits the signal enhancement to the materials' surface and subsurface layers, there is need for hyperpolarization approaches which will provide sensitivity in the bulk of micron sized particles. Recently, an alternative in the form of paramagnetic metal ions has emerged. Here we demonstrate the remarkable efficacy of Mn(II) dopants, used as endogenous polarization agents for MAS-DNP, in enabling the detection of ^{17}O at a natural abundance of only 0.038%. Distinct oxygen sites are identified in the bulk of micron-sized crystals, including battery anode materials $Li_4Ti_5O_{12}$ (LTO) and $Li_2ZnTi_3O_8$, as well as the phosphor materials $NaCaPO_4$ and $MgAl_2O_4$, all doped with Mn(II) ions. Density functional theory calculations are used to assign the resonances to specific oxygen environments in these phases. Depending on the Mn(II) dopant concentration, we obtain significant signal enhancement factors, 142 and 24, for ^6Li and ^7Li nuclei in LTO, respectively. We furthermore follow the changes in the $^{6,7}Li$ LTO resonances and determine their enhancement factors as a function of Mn(II) concentration. The results presented show that MAS-DNP from paramagnetic metal ion dopants provides an efficient approach for probing informative nuclei such as ^{17}O, despite their low gyromagnetic ratio and negligible abundance, without isotope enrichment.

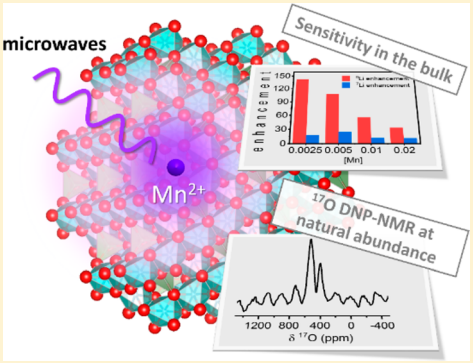

1. INTRODUCTION

Solid-state NMR (ssNMR) spectroscopy is an invaluable structural technique for probing short-range order and structure−function relations in materials science.[1−3] However, its main drawback is its low sensitivity. In recent years, with the advancement of high-field dynamic nuclear polarization (DNP) under magic angle spinning (MAS),[4,5] it has been demonstrated that ssNMR sensitivity can be increased by several orders of magnitude.[6,7] As such, MAS-DNP has been successfully implemented to study heterogeneous catalysts,[6,8−14] nanoparticles[15−17] and battery materials.[18,19] In particular, ^{17}O with a natural abundance of only 0.038% is an especially appealing target for hyperpolarization due to its high structural and chemical sensitivity[20,21] in oxides and inorganic surfaces[15,22,23] that are undetectable by standard ssNMR methods.

Sensitivity via DNP is achieved by transferring the high spin polarization of unpaired electrons to surrounding coupled nuclei by microwave (μw) irradiation. Typically, nitroxide radicals are added to diamagnetic samples as exogenous radical solutions and form a glassy matrix at the experimental cryogenic temperatures (~100 K).[7] This technique is robust and efficient for sensitivity gain; however, since the polarization spreads from the surface of the particles, it is most commonly applied to materials with high surface-to-volume ratio. While recently it was shown that nitroxides can also be used for polarization beyond the surface and subsurface layers of inorganic particles,[24] there is need to develop efficient alternative approaches to gain hyperpolarization in the bulk of micron sized inorganic particles, such as endogenous polarization sources, which may be advantageous in many materials systems.

Endogenous polarization in MAS-DNP can be achieved from paramagnetic metal ions. Their use for endogenous polarization has been demonstrated in biomolecules by Mn(II)

Received: October 12, 2018
Published: December 11, 2018

DOI: 10.1021/jacs.8b11015
J. Am. Chem. Soc. 2019, 141, 451−462

substitution in the metal binding active site[25] and in a Cr(III) doped molecular crystal in a metal−organic complex.[26] Similarly, in the early days of DNP, paramagnetic metal ion dopants and defect sites were utilized as endogenous polarization agents in the bulk of inorganic single crystals.[27−31] These experiments were performed on static samples at ultralow temperatures and low fields.

The utilization of paramagnetic metal ion dopants is an extremely appealing route for DNP in materials science: Metal ion dopants are routinely employed for introducing or improving material functions such as ionic and electronic conductivity, catalytic activity, and optical properties. In such systems dopants can serve an additional role, by acting as endogenous polarization agents for DNP they may provide the needed sensitivity to probe low sensitivity and/or low abundance nuclei. Alternatively, the established protocols for introducing metal ion dopants in important materials classes such as oxides, silicates, phosphates, and aluminates, provide a route for introducing dopants as "structural spies", incorporated in the material with control, at minute quantities, and with negligible interference with the material's structure and function. In the context of NMR sensitivity enhancement, paramagnetic metal ions are commonly introduced in the study of glasses to reduce the experiment time through shortening the nuclear spin relaxation.[32] We have recently demonstrated this concept for DNP, polarizing ^{7}Li nuclei in the bulk of micron sized $Li_4Ti_5O_{12}$ (LTO),[33] circumventing the addition of a solvent matrix. LTO is a promising battery anode material[34−40] which was shown to have improved ionic mobility and function upon doping with metal ions.[36,41] By doping LTO with Mn(II) ions and using the dopants as endogenous polarization agents in static, low field, DNP experiments, we were able to achieve more than 10-fold increase in signal intensity.

Here we expand this approach, demonstrating the high sensitivity achieved in the bulk of micron sized inorganic crystals in high field MAS-DNP experiments from endogenous Mn(II) dopants. MAS-DNP enhancements of up to ca.140 and 24 fold are obtained for ^{6,7}Li resonances from the bulk of Mn doped LTO (Mn-LTO).[42] Moreover, we show that Mn(II) based MAS-DNP provides sufficient sensitivity for detecting ^{17}O at natural isotopic abundance. ^{17}O DNP enhanced ssNMR spectra are acquired and assigned, supported by density functional theory (DFT) calculations, for titanate anode materials (Mn(II) doped LTO and $Li_2ZnTi_3O_8$), Mn(II) doped $NaCaPO_4$ phosphor, and Mn(II) doped $MgAl_2O_4$ phosphor and nuclear waste storage material.

We first describe the overall signal enhancement obtained for ^{6,7}Li in Mn-LTO samples for various Mn(II) contents, assign the different Li resonances, and determine their individual enhancement factors, revealing strong dependence and variation depending on the Mn(II) concentration. We then present ^{17}O spectra acquired at natural abundance in Mn-LTO and other oxides, enabled by DNP from endogenous Mn(II) dopants, establishing it as a powerful approach to investigate challenging nuclei in solids. Finally, we shortly discuss the mechanistic aspects of the DNP process from endogenous Mn(II) polarization.

2. METHODS

2.1. Materials. Samples of $Li_4Ti_5O_{12}$ doped with Mn ions were prepared by solid state synthesis as described previously.[33] A ^{6}Li enriched sample was prepared in the same way using 95% ^{6}Li enriched Li_2CO_3 as precursor (Sigma-Aldrich). All samples were characterized by X-ray diffraction and EPR spectroscopy (Figure S1 and ref 33). Four Mn(II) concentrations were studied here with a nominal Mn content of x = 0.0025, 0.005, 0.01, and 0.02 representing the mole ratio of Mn in the LTO formula of $Li_4Ti_5O_{12}$. These samples are labeled Mn0025, Mn005, Mn01, and Mn02, respectively.

Mn-doped $Li_2ZnTi_3O_8$, with 0.005 Mn per $Li_2ZnTi_3O_8$ formula, was prepared by standard solid-state reaction method. First, all of the reacting materials (Li_2CO_3 (Strem Chemicals, Inc. 99.99% purity), $MnCO_3$ (Alfa Aesar, 99.9% purity), ZnO(Alfa Aesar, 99.9%), and TiO_2 (Strem Chemicals, Inc. 99.99% purity) were dried in an oven at 80 °C for a few hours. Then these materials were mixed by grinding, pelletized, and fired in a box-furnace at 750 °C for 6 h in open air followed by firing at 1100 °C for 3 h with one intermediate grinding. 5% excess Li_2CO_3 was taken in the mixture to compensate for lithium evaporation during calcination at the elevated temperature.

Mn-doped $MgAl_2O_4$, with 0.001 Mn per $MgAl_2O_4$ formula, was prepared in accordance to a published solid state reaction.[43] The starting materials—MgO (Strem Chemicals, Inc. 99.9% purity), Al_2O_3, and $MnCO_3$ (Alfa Aesar 99.985% purity)—were mixed by ball-milling for 1 h and then pelletized and calcined in air at 1400 °C for 6 h. Mn-doped $NaCaPO_4$, with 0.002 Mn per $NaCaPO_4$ formula, was prepared by solid state reaction.[44] The starting materials were $CaCO_3$ (Alfa Aesar 99.999%), $NH_4H_2PO_4$ (Strem Chemicals, Inc. 99.998% purity), $MnCO_3$ (Alfa Aesar 99.985% purity), and Na_2CO_3. The mixture was heated to 350 °C for 10 h. The obtained powder was mixed by ball-milling for 1 h, pelletized and heated to 750 °C for 8 h in air. After that, the sample was thoroughly mixed by mortar and pestle, pelletized, and heated to 900 °C for 10 h in a tube furnace under $N_2\backslash H_2$ (5%) flow.

All materials were characterized by X-ray powder diffraction to determine their phase purity.

2.2. MAS-DNP Experiments. DNP experiments were performed on a Bruker 9.4 T Avance-Neo spectrometer and a Bruker Avance III spectrometer equipped with a sweep coil and a 263 GHz gyrotron system. A 3.2 mm triple resonance low temperature (LT)-DNP probe was used for the experiments at MAS of 10 kHz. All experiments were performed around 100 K with sample temperature of about 98 and 107 K without and with μw irradiation, respectively. For all ^{6,7}Li and ^{17}O measurements single pulse excitation was used following a train of saturation pulses and delay for relaxation or polarization build-up. The RF amplitudes used were 50, 87, and 83 kHz for ^{17}O, ^{7}Li, and ^{6}Li, respectively. Longitudinal relaxation, T_1, and polarization build up time with μw irradiation, T_{bu}, were measured with the saturation recovery pulse sequence using a train (150 repetitions) of short pulses separated by 1.5 ms (for ^{6}Li and ^{17}O) and 1 ms (for ^{7}Li) for saturation. A MATLAB code was used to fit the individual ^{7}Li spectra and fit the integrated signal intensity with exponential functions. ^{6}Li relaxation experiments were analyzed using TOPSPIN and fitted with ORIGIN. DMFIT[45] was used for spectral deconvolution and determination of enhancement factors of individual resonances. Overall signal intensity and enhancement factors were determined by integration over the entire range of resonances in TOPSPIN. Chemical shift referencing of ^{6,7}Li was performed using secondary references of Li_2CO_3, set at 0 ppm at room temperature. ^{17}O shifts were referenced to ^{17}O enriched Li_2O or H_2O (natural abundance) set at 35 ppm[46] and 0 ppm, respectively. The RF amplitudes for ^{17}O were determined from nutation experiments on ^{17}O enriched Li_2O or H_2O and the pulse length was scaled by a factor of 3 in MAS-DNP experiments.

2.3. EPR Spectroscopy. Field sweep echo detected pulsed EPR experiments were performed on Mn doped LTO on a home-built pulsed W band (95 GHz) spectrometer at 25 K. The Mn(II) line shape at W band was fitted using EASYSPIN code.[47] These parameters were then used to simulate the line-shape at 9.4 T (neglecting any line width changes due to relaxation). All other Mn doped phases were characterized at room temperature with continuous wave (CW) EPR at X-band.

2.4. DFT Methodology. Electronic structure calculations were performed for LTO, $Li_2ZnTi_3O_8$, $MgAl_2O_4$, and $NaCaPO_4$ using two

DOI: 10.1021/jacs.8b11015
J. Am. Chem. Soc. 2019, 141, 451−462

different density functional theory (DFT) simulation packages: the plane-wave pseudopotential Vienna Ab Initio Simulation Package (VASP)[48−50] and the all-electron mixed plane-wave/orbital WIEN2k package.[51,52] The Perdew, Burke, and Ernzerhof (PBE) exchange-correlation (XC) functional of the generalized gradient approximation (GGA)[53] type was used in all calculations. The number of atoms in the supercells for LTO, $Li_2ZnTi_3O_8$, $MgAl_2O_4$, and $NaCaPO_4$ were 168, 56, 56, and 84, respectively.

2.4.1. Geometry Optimizations and Self-Consistent Field Calculations. For the plane-wave pseudopotential calculations using VASP, we employed an energy cutoff of 600 eV for the plane wave basis set expansion and the projector augmented wave (PAW) methodology was adopted to define the core electrons.[54] The self-consistent field and density of states calculations for the full supercells for all systems employed the Monkhorst−Pack scheme[55] with Brillouin zone (BZ) k-point grids as described in Table S7. All system ionic positions and unit cell parameters were relaxed until the net Hellmann−Feynman force per atom was less than 0.01 eV/Å.[56]

We also employed the WIEN2k package to perform all electron DFT calculations. All calculations were based on the LAPW+lo method, with the core electron states separated from the valence states at −6.0 Ry. The calculations were converged for a plane wave cutoff given by the factor $R_{MT}K_{MAX} = 7$, where R_{MT} is the smallest atomic sphere radius and K_{MAX} is a cutoff for the basis functions wave vector.

Test calculations were performed to determine the required number of *k*-points in the irreducible Brillouin zone to achieve convergence for the final NMR results for all systems.

Li_2O was used as a reference for ^{17}O NMR shift calculations, with a value of 35 ppm.

Further details for all calculations are provided in Table S7.

2.5. EXAFS Measurements and Analysis. Mn K-edge X-ray absorption fine structure (XAFS) measurements were performed at the ISS beamline of the National Synchrotron Light Source-II (NSLS-II) at Brookhaven National Laboratory, and Ti K-edge, at the beamline BL2-2 at Stanford Synchrotron Radiation Lightsource (SSRL) at SLAC National Accelerator Laboratory. For Ti K-edge measurement in transmission mode, the sample powder was mixed with boron nitride. Mn K-edge data were measured in fluorescence, using a multielement silicon drift detector (SDD), and 20 scans were averaged to improve the signal-to-noise ratio.

To analyze Extended XAFS (EXAFS) data, the nonlinear least-squares fitting to theoretical FEFF6 model, as implemented in Demeter package,[57] was applied. Data from Ti K- and Mn K-absorption edges were fitted up to the second coordination shell from Ti and Mn, respectively, using the spinel structure as a reference for theoretical calculations of photoelectron scattering amplitudes and phase shifts. For Mn edge data analysis, several models were compared, in which Mn absorbers were placed in different sites in the spinel lattice. In one model, described below, Mn atoms substituted Ti atoms at the octahedral lattice sites, while in the second model, at the tetrahedral sites. The fitted variables were amplitude reduction factors S_0^2, corrections ΔR to the model interatomic distances, the bond length disorder factors (σ^2) for Ti/Mn−O and Ti/Mn−Ti pairs, as well as the corrections ΔE_0 to the photoelectron energy origin. For the tetrahedral Mn model, in addition, the third nearest neighbor Mn−O contribution was refined in the fit as well.

3. RESULTS AND DISCUSSION

3.1. DNP Enhancement Profiles. A series of Mn-doped LTO compounds with Mn(II) content of $x = 0.0025$, 0.005, 0.01, and 0.02, representing the mole ratio of Mn in the LTO formula of $Li_4Ti_5O_{12}$, was synthesized and characterized in previous work, where the homogeneous introduction of Mn(II) ions to the lattice was demonstrated.[33] These samples are labeled Mn0025, Mn005, Mn01, and Mn02, respectively. Here, we examined the Mn-doped LTO samples with high-field MAS-DNP.

The MAS-DNP field-swept enhancement profiles of the Mn005 sample, measuring the enhancement factor $\varepsilon_{on/off}$ as a function of the magnetic field, were collected for $^{6,7}Li$ (Figure 1b,c). The profiles have an intricate structure, reflecting the

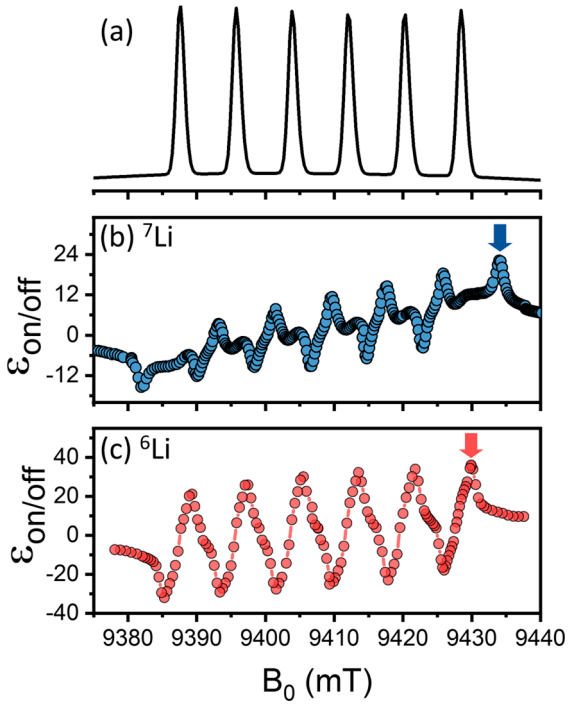

Figure 1. (a) Simulated pulse EPR spectrum of Mn005 sample at 9.4 T and electron frequency of 263.5 GHz. Simulation parameters and experimental spectrum at W band are given in the SI. (b) ^7Li DNP sweep profile acquired with a build-up time of 10 s for Mn005. (c) ^6Li DNP sweep profile acquired with a build-up time of 20 s for Mn005. The arrows mark the optimal field position for maximal enhancement.

EPR spectrum of Mn(II) (Figures 1a and S1). The strong hyperfine coupling of Mn(II) electron spin (S = 5/2) with its ^{55}Mn nucleus (I = 5/2) causes the characteristic splitting of the narrow $m_s = -1/2$ to $m_s = +1/2$ central transition to six transitions, with a coupling constant of ca. 229 MHz, similar to values previously reported for Mn(II).[58] Each line of the hyperfine sextet gives rise to negative and positive DNP enhancements. For ^7Li, the enhancement pairs overlap since its Larmor frequency (ω_n =155.5 MHz) is larger than half of the hyperfine coupling constant of Mn(II). This results in some interference between the positive and negative enhancements from adjacent transitions in the hyperfine manifold. In comparison, the DNP conditions for ^6Li (ω_n = 58.9 MHz) are better resolved and are more symmetric in intensity. The optimal condition for DNP enhancement for both ^6Li and ^7Li occurs at higher fields, at the position marked with an arrow (Figure 1b,c). It should be noted, however, that the measurements were not performed at steady state conditions for polarization build up. Furthermore, the sweep profile does not cover the entire DNP range as the signal does not return to its thermal polarization value of $\varepsilon_{on/off} = 1$ at the outermost field positions measured here.

The DNP sweep profile can provide some insight into the dominating mechanism of the polarization transfer process. The maxima and minima of both ^6Li and ^7Li sweep profiles (Figure 1b,c) are separated by twice their Larmor frequency ($2\omega_n$). This suggests that the dominant DNP process is via

DOI: 10.1021/jacs.8b11015
J. Am. Chem. Soc. 2019, 141, 451−462

solid effect (SE, by an electron−nucleus pair) according to the matching condition of $\omega_{\mu w} = \omega_e \pm \omega_n$, where $\omega_{\mu w}$ is the μw frequency and ω_e is the Larmor frequency of the electron.[5]

We note, however, that the dopant concentration in mM in these samples is between 20 and 150 mM (see the Supporting Information), a concentration regime that was shown to have cross effect (CE) contribution in Gd(III) and Mn(II) metal complexes as exogenous polarizing agents.[58] In addition to high concentration, which makes electron−electron couplings likely, the resonance frequency separation between the two electrons, $\Delta\omega_e$, should satisfy the CE condition $\Delta\omega_e = \omega_n$. Considering that the hyperfine split sextet lines of the $m_s = -1/2$ to $+1/2$ transition are much narrower than both ^{6,7}Li Larmor frequencies, it is unlikely that CE occurs between resonances within this manifold. Nevertheless, it may be possible that CE is contributing to the DNP enhancement through electron pairs where one (or both) electron is populating higher electron spin transitions (with $|m_s| > 1/2$).

3.2. ^{6,7}Li Signal Enhancement and Dependence on Mn(II) Concentration. Polarization build-up times, T_{bu}, were measured at the optimal field positions (marked with arrow in Figure 1b,c) for ^{6}Li and ^{7}Li. For each Mn(II) content, overall $\varepsilon_{on/off}$ factors were determined from the ratio of the integrated area of the entire spectrum with and without μw at steady state conditions ($5T_{bu}$). Significant enhancements were obtained for both ^{6}Li and ^{7}Li, which varied strongly with Mn(II) dopant concentration (Figure 2). The insets show a comparison between the Li spectra acquired with and without microwave irradiation. The highest enhancement for ^{6}Li was 142 fold in the sample with lowest Mn(II) content, M0025, and it decreased with higher concentrations of Mn(II) dopant. Generally, the enhancement was significantly higher for ^{6}Li compared to ^{7}Li. For ^{7}Li, the highest enhancement was 24-fold obtained in Mn005. When considering the ratio between the gyromagnetic ratios of the two lithium isotopes ($\gamma^7_{Li}/\gamma^6_{Li} = 0.38$), the enhancement obtained for ^{6}Li is only a factor of 2 higher than that of ^{7}Li. This difference could be due to an interplay of the polarization transfer mechanism, the nuclear spin-lattice relaxation times (T_{1n}) and the natural abundance of the nuclei. The T_{1n} and T_{bu} of ^{6}Li are higher by 2 orders of magnitude compared to ^{7}Li (see next paragraphs), such that a higher degree of hyperpolarization can be achieved for ^{6}Li, resulting in higher enhancement values.[59] In the case of ^{6}Li, the hyperpolarization spreads over a smaller spin bath (7% natural abundance), which furthermore supports higher ^{6}Li enhancement in comparison to ^{7}Li.

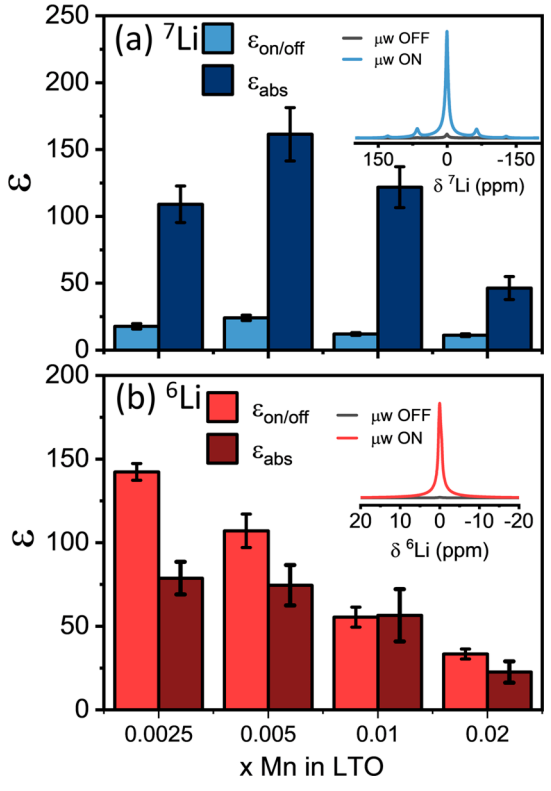

Figure 2. MAS-DNP signal enhancement factors for (a) ^{7}Li and (b) ^{6}Li obtained at the optimal field position and steady state conditions ($5T_{bu}$) as a function of the Mn(II) concentration in LTO. The different enhancement factors are described in the text. The insets show the μw on and off spectra for Mn005 (^{7}Li) and Mn0025 (^{6}Li).

In order to have a better estimation of the absolute gain in sensitivity achieved from Mn(II) dopants in MAS-DNP, we must take into account effects of paramagnetic quenching by the Mn(II) dopants and/or depolarization, the change in experiment time due to relaxation enhancement by Mn(II) doping, and the gain in sensitivity due to the temperature change to 100 K.[60−63]

To this end, we performed a quantitative measurement of the ^{7}Li resonances by recording the steady state LT NMR spectra with a relaxation delay of $5T_1$ in Mn-doped and undoped LTO (Figure S2). Up to Mn(II) content of $x = 0.005$ there was no significant change in the integrated signal intensity. However, at higher Mn(II) concentrations we observe a decrease in the Li signal of the μw off spectra. This loss of intensity is due to signal quenching (and possibly depolarization if there is any contribution from CE) in the presence of the paramagnetic Mn(II).[63−65] Additionally, as the dopant concentration increased, the T_{1n} measured decreased and so did the T_{bu}. Both time constants were measured for ^{7}Li: in pure LTO, T_{1n} was 132 ± 4 s, while for Mn0025 the T_{1n} decreased dramatically and two components were evident originating from two spectral components, a longer T_{1n} of 8.9 ± 0.8 s and a shorter T_{1n} of 4.7 ± 0.2 s (Figure S3 and Table S1). Similar values were measured for Mn005 for the longer T_{1n} component, 8 ± 1 s, and a shorter component of 2.3 ± 0.6 s, while for Mn01 the longitudinal relaxation times decreased by roughly a factor of 2. Overall, across all samples, for a given Mn(II) concentration, the values measured for T_{1n} and T_{bu} for ^{7}Li were the same within error.

The effects of signal quenching (given by the ratio between the integrated signal intensity of the doped and undoped samples, Θ) and the difference in T_{1n} and T_{bu} on enhancement were taken into account by the calculation of $\varepsilon_{abs} = \varepsilon_{on/off}\,\Theta(T_{1,undoped,RT}/T_{bu})^{1/2}\,\chi_T$. Here we took into account the T_{1n} of the undoped LTO sample at room temperature ($T_{1,undoped,RT}$) and χ_T defined as the gain in sensitivity due to the LT measurements.[60] For ^{7}Li, the significantly shorter $T_{1,bu}$ in doped samples, even at low temperatures, as compared with the RT T_{1n} of 29 ± 1 s for LTO, yields an increase of 1 order of magnitude in ε_{abs} factors relative to $\varepsilon_{on/off}$. For ^{6}Li, however, we observed an increase of 2 orders of magnitude in build-up times compared to the RT T_{1n} of the undoped sample (56 ± 8 s). In Mn0025, the polarization build-up curve was best fitted with two T_{bu} components, 3100 ± 200 and 290 ± 30 s, while in Mn02 they were best fitted by three T_{bu} components of 1600 ± 300, 60 ± 10, and a shorter component of 6 ± 1 s

DOI: 10.1021/jacs.8b11015
J. Am. Chem. Soc. 2019, 141, 451−462

(Figure S4 and Table S2). This resulted in decrease in the absolute signal gain for this isotope.

A careful examination of the different lithium spectra as a function of the Mn(II) concentration reveals several Li environments, the structural origin of these as well as the individual enhancement factors will be discussed in the next section.

3.3. Lithium Environments and Their Enhancement in the Presence of Mn(II) Dopants. The incorporation of Mn(II) within the LTO lattice was demonstrated by XRD and EDS.[33] As the bonding and environment of the site doped by Mn(II) ions can affect the Li resonances observed in NMR, additional structural characterization was performed with extended X-ray absorption fine structure (EXAFS). The Fourier transform magnitude of the EXAFS spectrum, acquired at the Mn K-edge, is shown in Figure 3. The first two peaks in

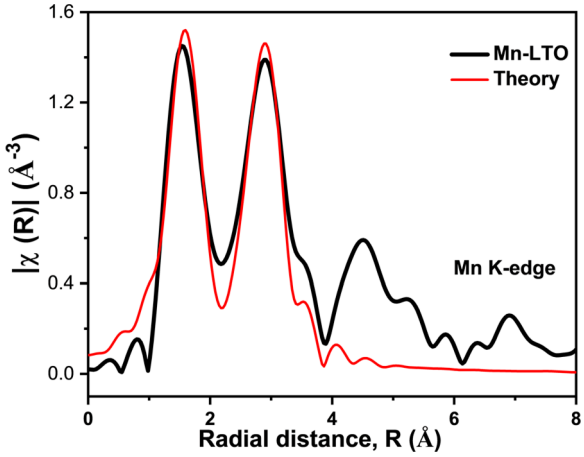

Figure 3. Fourier transform magnitude of the data and FEFF6 fit for Mn K-edge EXAFS spectrum for Mn01 sample. The fitting was performed by assuming Mn(II) substitution for tetrahedral Li sites, in the *k*-range from 2.0 to 9.0 $Å^{-1}$ and *R*-range from 1.25 to 3.92 Å.

r-space correspond to Mn−O and Mn−Ti closest distances. The spectrum was fitted using the structure reported for undoped LTO[66] in which Mn(II) ions were placed at either Ti (octahedrally coordinated) or Li (tetrahedral) sites. Based on the comparison of the fitting results and the qualities of the fit obtained for different models, we conclude that Mn(II) is doped predominantly in Li tetrahedral sites (Figures 3 and S5 and Table S3).

We now turn to discuss the different environments in the lithium spectra, their spectral assignment, and their individual enhancement factors in DNP.

3.3.1. ^{7}Li Spectra. The resonance frequencies observed for Li are within the typical range of Li NMR of diamagnetic materials (about −5 to +5 ppm).[67,68] Considering first only the ^{7}Li spectra, while a single Li resonance at 0.1 ppm was observed for the undoped LTO, with the introduction of Mn(II) a second broad Li resonance appeared in the spectrum centered at about 0 ppm. The width and contribution of this resonance increased with Mn(II) concentration (Figures 4 and S3) and in Mn02 it accounts for 50% of the integrated intensity. Furthermore, while the narrow and broad resonances have similar $\varepsilon_{on/off}$ enhancement factors at low Mn(II) concentrations (Figure 4b) and both reach their highest polarization in Mn005, the broad component was enhanced more significantly at higher Mn(II) concentrations.

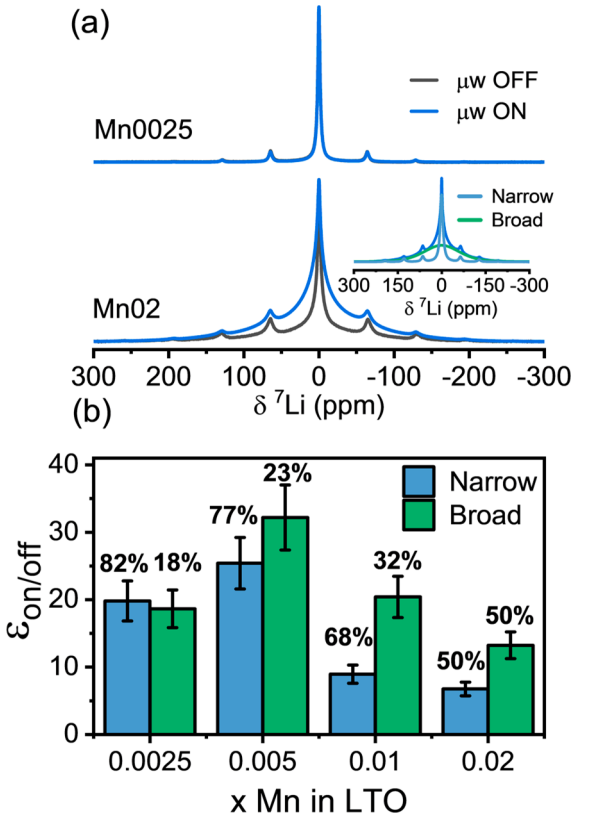

Figure 4. (a) ^{7}Li LT MAS spectra acquired with and without DNP for Mn0025 and Mn02. Inset: spectral deconvolution for the Mn02 sample (spectra were normalized for comparison). (b) MAS-DNP enhancement factors for the two ^{7}Li spectral components (fractions of the two components for each Mn(II) concentration are marked in %).

3.3.2. ^{6}Li Spectra. Higher resolution was achieved in the ^{6}Li spectra due to the lower gyromagnetic ratio and low natural abundance, resulting in weaker dipolar coupling (with the surrounding nuclei and unpaired electrons) and lower quadrupole coupling strength of the ^{6}Li isotope compared to ^{7}Li. The ^{6}Li spectrum of undoped LTO (Figures 5 and S9), contains two overlapping resonances at 0.1 and −0.3 ppm which can be assigned to Li at the tetrahedral sites (Td) and octahedral sites (Oh) respectively.[69] A ratio of approximately 3:1 is observed at room temperature measurements indicating the undoped spinel is formed with the expected stoichiometry ($[Li]-[Li_{1/6}Ti_{5/6}]_2O_4$ following the standard AB_2O_4 spinel structure). As the concentration of Mn(II) increases, the fraction of these two resonances decreases, and two additional overlapping environments are detected (Figure 6b): a broad peak centered at 0 ppm and a narrow peak at ∼−1 ppm. The broad resonance becomes more prominent as Mn(II) ions are introduced into the LTO lattice and increases to a relative amount of 50−60% in Mn01 and Mn02, accompanied by a decrease in the two sharp Li Td and Oh environments. This suggests that the broad resonance is correlated with the Mn(II) content and may arise from Li sites in proximity to the Mn(II) ions. This assignment is further supported by the broadening observed with Mn(II) content, which may be due to faster transverse relaxation and/or increase in local disorder and heterogeneity around the Mn(II) dopants as well as dipolar coupling to multiple Mn(II) dopants. We note that no significant Fermi contact shifts were observed for this broad resonance. Pigliapochi et al. calculated the Fermi contact shifts

DOI: 10.1021/jacs.8b11015
J. Am. Chem. Soc. 2019, 141, 451−462

3.3.2 ^{6}Li spectra

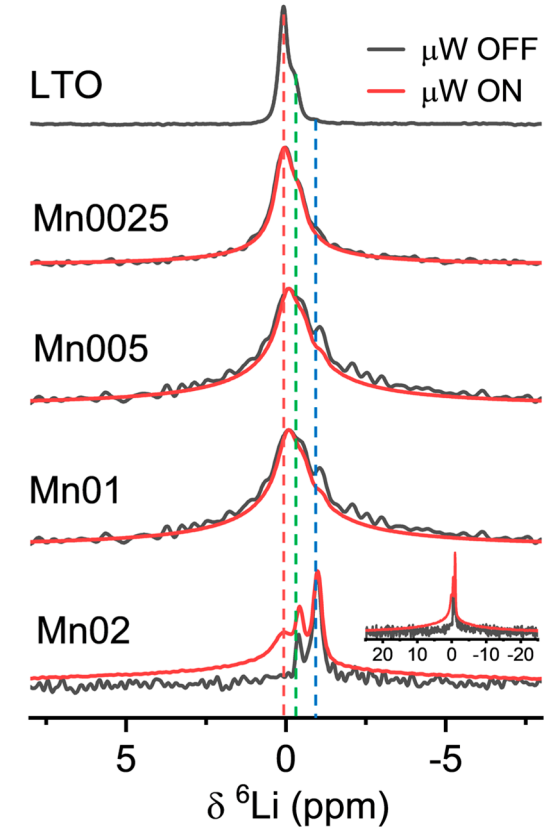

Figure 5. ^{6}Li LT MAS spectra acquired with and without DNP (spectra were normalized for comparison) for Mn-doped samples at steady state ($5T_{bu}$). The spectrum of the undoped LTO was acquired at RT due to the extremely long T_1 at 100 K. Inset: spectrum of Mn02 displaying a broader range.

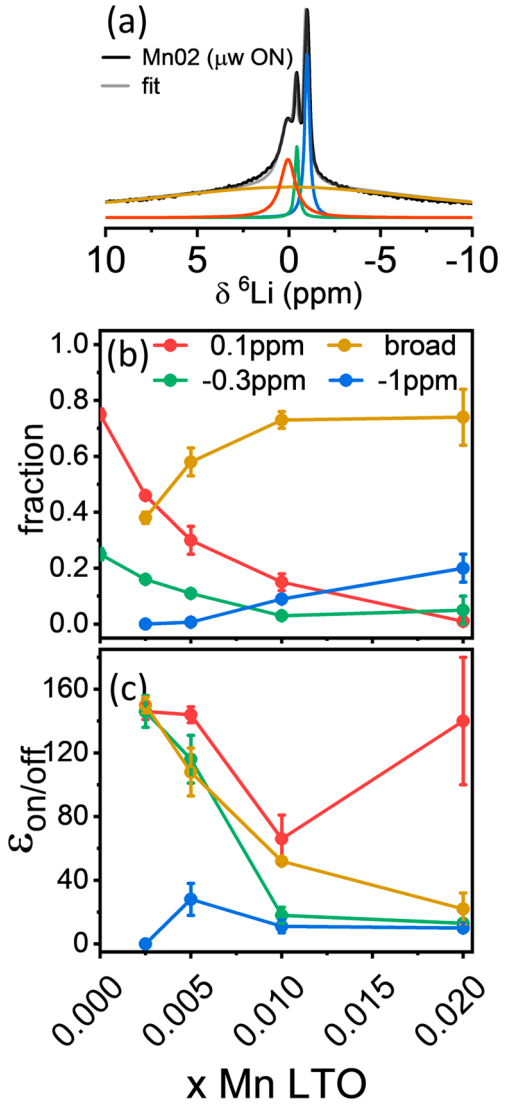

Figure 6. (a) Spectral deconvolution of the MAS-DNP spectrum of Mn02 sample. (b) The fraction of the four spectral components obtained from the deconvolution of the μw OFF spectra as a function of Mn(II) content. (c) Signal enhancement factors calculated for the four spectral components.

expected for Li in both tetrahedral and octahedral sites coordinated to Mn(II) via oxygen.[70] They found relatively small shifts of 28 ppm for Li in Td sites (coordinated to Mn(II) in Oh sites) and 17 and 64 ppm for Li in Oh sites (coordinated to Mn(II) in Td and Oh sites, respectively). While these shifts are within the range spanned by the broad resonance in our samples, it is unlikely that the Li sites in the first coordination shell of the paramagnetic Mn(II) (bonded to Mn(II) via oxygen) contribute to the broad resonance as these are most likely quenched in the Mn01−02 samples. In the samples with lower Mn(II) content, they might be quenched or below the detection limit.

As expected, with the increase in Mn(II) concentration, we observe significant signal loss. Taking into account the EXAFS results, indicating that Mn(II) ions occupy Td sites (assuming this is valid for all the Mn(II) concentrations), along with the fraction of ^{7}Li signal quenched at different Mn(II) concentrations, we can estimate the range of quenching and/or depolarization around the Mn(II) dopants (Figure S6). Using a random distribution model for the dopants, we expect that for x = 0.01 and 0.02 Li ions within a radius of 10 and 14 Å, respectively, around the Mn(II) are not detected. We note that this range will be smaller for ^{6}Li, which has a lower quenching factor. In the samples with lower Mn(II) content, where we do not observe significant signal quenching, our results are not sufficiently accurate to determine whether signal quenching is present. Nevertheless, if quenching does occur in these samples it can only affect environments at a radius below 6 Å around the Mn(II) dopants (constituting 3−6% of the Li in the sample, including the Li resonances in the first coordination shell, which is within the measurement error of the spectral quantification).

Additionally, the relative contribution of the new environment at ∼−1 ppm increases up to 20% of the signal intensity going from Mn005 to Mn02. According to its chemical shift, this new environment may correspond to monoclinic Li_2TiO_3 impurity phase,[69,71] which is a common impurity in LTO,[42,69] initiated by the presence of excess Li precursor, as extensively discussed in ref 42. Measurement of the RT ^{6}Li spectrum of monoclinic Li_2TiO_3 confirmed the assignment to this impurity phase (Figure S8a). Additional support for this assignment is given by the ^{6}Li spectrum of the undoped LTO at RT (Figure S9) and the results of a 2D double quantum (DQ) correlation experiment performed on a ^{6}Li enriched Mn005 sample (Figure S10).

DOI: 10.1021/jacs.8b11015
J. Am. Chem. Soc. 2019, 141, 451−462

Interestingly, the resonances from the Li_2TiO_3 impurity also undergo signal enhancement which might indicate that this phase is well dispersed within the doped LTO framework or that it is also doped, to some extent, by Mn(II) ions. The significant reduction in signal intensity in Mn01 and Mn02 samples due to quenching causes the contribution of Li_2TiO_3 to appear more dominant in higher Mn(II) concentrations and makes quantification of the impurity phase across all Mn(II) concentrations impossible. However, based on powder diffraction (Figure S11) we estimate its contribution by 4−10% in all samples (4% in the undoped LTO and 8−10% in the Mn01 and Mn02 samples, respectively).

3.4. Natural Abundance ^{17}O Detection via MAS-DNP.

3.4.1. Natural Abundance ^{17}O Spectra of LTO. Next we confirm the feasibility of acquiring ^{17}O DNP enhanced NMR spectra at natural abundance by utilizing the endogenous Mn(II) polarization. Remarkably, with MAS-DNP, a ^{17}O spectrum was acquired at natural abundance within a day of measurement for Mn005 (Figure 7a). The ^{17}O spectrum was

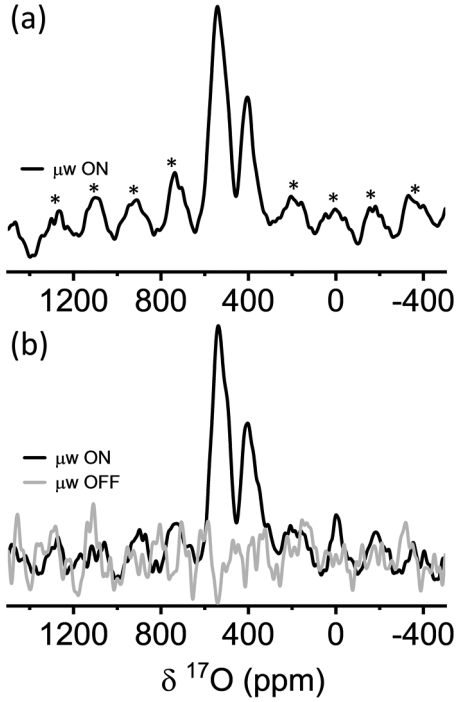

Figure 7. (a) MAS-DNP natural abundance ^{17}O spectrum acquired for Mn005. 1600 scans were collected with a build-up time of 60 s. Two isotropic resonances are labeled, flanked by a manifold of spinning sidebands (marked with asterisks). (b) Comparison of a μw ON and OFF spectra acquired with a build-up and relaxation time of 170 s, respectively, and 64 scans.

acquired at the optimal field for ^6Li in the DNP sweep profile, with a slight correction due to the small difference in Larmor frequencies of ^{17}O and ^6Li (ω_n = 54 and 58.9 MHz, respectively). In comparison, there was no observable signal with μw off (Figure 7b).

Two oxygen environments were observed, at 536 and 403 ppm, with no distinct second order quadrupole line-shape. This may indicate that the quadrupole coupling frequency is lower than the broadening due to relaxation and/or disorder in the material as well as the dipolar couplings to the paramagnetic Mn(II) ions. Further insight into these oxygen sites was obtained from DFT calculations.

3.4.2. DFT Calculations of ^{17}O NMR Parameters in LTO. For the calculations we considered the undoped LTO spinel structure ($Fd\bar{3}m$ space group) with eight formula units of $[Li]_{8a}[Ti_{5/3}Li_{1/3}]_{16d}[O_4]_{32e}$ in its unit cell.[72] We investigated five low energy configurations (C1−C5, Table S5−S6).[72] In particular, configurations C1 and C2 were considerably more stable than all others considered. The supercell structure and total ground state energy of these configurations are shown in Figure 8a,b and Table S5−S6, respectively.

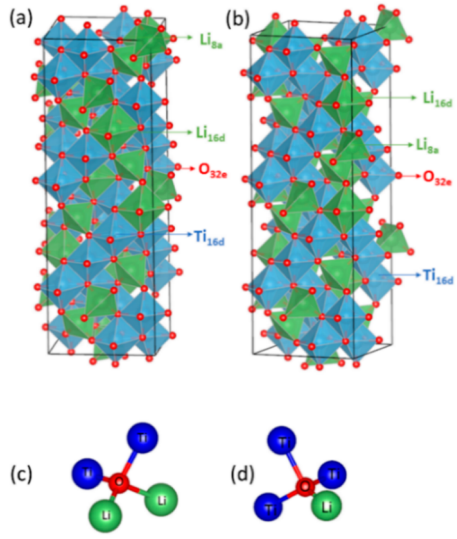

Figure 8. Supercells of $Li_4Ti_5O_{12}$ for two configurations, C1 and C2, are shown in panels a and b, respectively. The tetrahedral oxygen is surrounded by (c) two Li-ions and two Ti-ions ($O@Li_2Ti_2$) and (d) one Li-ion and three Ti-ions ($O@LiTi_3$).

First-principles calculations of chemical shielding tensors and nuclear quadrupole coupling constants for the most stable LTO configurations (C_1 and C_2) were computed using the PBE functional and GIPAW method within the VASP and WIEN2k codes.[73,74] In our supercell crystal structure, we observed two types of oxygen environments, which are shown in Figure 8c,d. The computed NMR chemical shifts of LTO are shown in Table 1. The isotropic shielding was computed,

Table 1. Calculated Average Values of NMR Chemical Shifts and EFG Parameters for O Sites in LTO Spinel[a]

configuration	types of O	δ_{iso}^{Cal} (ppm) (VASP, WIEN2k)	C_q (MHz)	η	δ_{iso}^{2Q} (ppm)
C_1	$O@Li_2Ti_2$	556, 644	0.71	0.571	−1.1
	$O@LiTi_3$	448, 468	−0.042	0.612	0
C_2	$O@Li_2Ti_2$	554, 599	0.760	0.535	−1.3
	$O@LiTi_3$	446, 509	0.211	0.702	−0.1

[a]The computed values for $O@Li_2Ti_2$ and $O@LiTi_3$ were averaged over 47 and 49 oxygen atoms, respectively.

with both VASP and WIEN2k, as the average chemical shifts within a LTO structure for a specific type of local oxygen environment, i.e., $O@Li_2Ti_2$ and $O@LiTi_3$. As can be appreciated from Table 1, the calculated values for both low energy configurations are fairly close to the experimental values of 403 (assigned to $O@LiTi_3$) and 536 ppm (assigned to $O@Li_2Ti_2$). We also show the histograms of all oxygens in the C_1 configuration in Figure S15. The contribution of isotropic

DOI: 10.1021/jacs.8b11015
J. Am. Chem. Soc. 2019, 141, 451−462

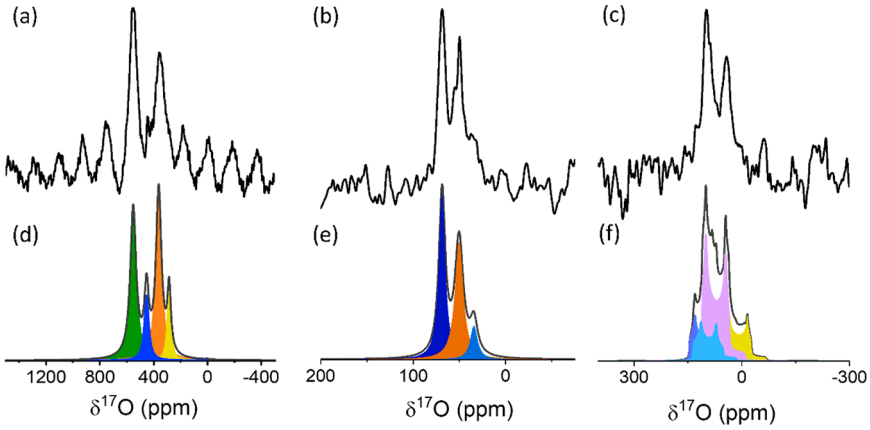

Figure 9. ^{17}O MAS-DNP spectra at natural abundance acquired with single pulse excitation. (a) Mn005 Li_2ZnTiO_3: 992 scans were collected with a build-up time of 60 s. (b) Mn001 $MgAl_2O_4$: 3258 scans were collected with a build-up time of 60 s. (c) Mn002 $NaCaPO_4$: 2514 scans were collected with a build-up time of 60 s. Fits for the ^{17}O spectra (d) Mn005 Li_2ZnTiO_3: four distinct oxygen resonances are observed at 550 ppm (green, 38 ± 2%), 451 ppm (blue, 12 ± 2%), 361 ppm (orange, 40 ± 3%), and 284 ppm (yellow, 10 ± 2%). (e) Mn001 $MgAl_2O_4$: three distinct oxygen resonances are observed at 69 ppm (navy blue, 46 ± 5%), 50 ppm (brown, 43 ± 6%), and 34 ppm (blue, 11 ± 4%). (f) Mn002 $NaCaPO_4$: Four overlapping oxygen resonances are observed at 155 ppm (blue, C_q = 5 MHz, η = 0.21, 10 ± 4%), 143 ppm (light blue, C_q = 5 MHz, η = 0.3, 11 ± 6%), 122 ppm (purple, C_q = 5.1 MHz, η = 0.14, 57 ± 6%), and 61 ppm (yellow, C_q = 5 MHz, η = 0.18, 22 ± 2%).

quadrupolar shift to the total isotropic resonance frequency can be neglected (Table 1, histograms in Figure S16).

Thus, our DFT calculations suggest that the two DNP enhanced ^{17}O resonances (Figure 7a) correspond to two dominant O environments in the low energy configurations. Surprisingly, these two environments have almost equal probabilities in the calculated structures while experimentally higher integrated intensity is observed for the resonance of O@Li_2Ti_2 (536 ppm; see Figure S12). This discrepancy may be explained by the relatively short polarization build-up times of 60−170 s, which most likely are far from steady state polarization. Thus, if the two oxygen sites differ in their build up times this can lead to different polarization efficiency and variations in their relative intensity. Another possibility is that the slight difference in quadrupolar coupling results in different RF excitation efficiency for the two sites.

To determine whether the Li_2TiO_3 impurity phase contributes to the ^{17}O spectrum, we have also computed the NMR chemical shifts for this phase. The computed chemical shifts for O@Li_2Ti_2 were 403 and 409 ppm and for O@$LiTi_3$ 371 and 334 ppm using VASP and WIEN2k, respectively. These match well with previously measured experimental values of 406 and 372 ppm.[75] Thus, we did not observe significant contribution of this phase in the ^{17}O spectrum.

3.4.3. Natural Abundance ^{17}O MAS-DNP Detection in Other Oxides. To demonstrate that ^{17}O detection at natural abundance is applicable in other oxides via endogenous DNP from Mn(II) dopants, we investigated three additional materials.

In a second titanate anode material, $Li_2ZnTi_3O_8$, doped with 0.005 Mn(II) ions per stoichiometric formula (resulting in Mn(II) concentration of 56.6 mM, see the Supporting Information), four ^{17}O resonances were observed in the MAS-DNP spectrum in less than a day of acquisition (Figures 9a and S19). These resonances, at 550, 450, 360, and 290 ppm (fit shown in Figure 9d, based on the echo experiment in Figure S19), match very well the ^{17}O environments expected from DFT calculations (Table S8 and Figure S17). The signal intensity, resonance frequencies and lack of quadrupolar broadening, all support the formation of a highly symmetric structure due to Li(I), Zn(II), and Ti(IV) cation ordering in the spinel lattice.[76] Another example where ^{17}O resonances provide insight into cation ordering is in the $MgAl_2O_4$ spinel. In this spinel it is useful to determine the degree of cation mixing for rationalizing and controlling material properties and in particular predicting and rationalizing its radiation tolerance.[77] The ^{17}O MAS-DNP of the Mn-doped phase (here with 0.001 Mn(II) corresponding to 25.2 mM, see the Supporting Information), which is also active as a phosphor material,[43] revealed at least three distinct ^{17}O resonances (Figure 9b,e). ^{27}Al MAS NMR measurement (Figure S21) was used to determine that one out of seven Al(III) ions mix with Mg(II) cations. DFT calculations performed for $MgAl_2O_4$, considering the degree of cation mixing, showed that three distinct O environments are expected within this range of frequencies (Figure S17). While in this specific spinel phase ^{27}Al ssNMR is a sensitive probe for local order,[78] ^{17}O may provide additional insight into the structure[79] and can be used to develop this approach for probing cation disorder in other phases which do not contain structurally sensitive nuclear spins.

The third system where we tested this approach for sensitivity enhancement is the phosphor material Mn(II) doped $NaCaPO_4$ (doped with 0.002Mn(II) per formula, corresponding to 39.4 mM, see the Supporting Information). According to the crystal structure, the undoped phase contains 12 inequivalent ^{17}O sites which were expected to result in measurable quadrupolar interactions due to their low symmetry. Indeed, the ^{17}O MAS-DNP spectrum contains several overlapping resonances (Figure 9c) which were analyzed by DFT calculations. The 12 distinct oxygen sites may be separated into four types of environments based on interatomic distances: O@PNa'_3Ca_2, O@PNa_2Ca_2, O@$PNaCa_2$, and O@PNa_3Ca_2. Here, the Na'_3 in the first environment corresponds to two tightly and one loosely coordinated Na^+ ion. The four O environments had significant quadrupole couplings of about 5 MHz resulting in severe overlap in a 1D spectrum (fit in Figure 9f, based on the calculated DFT parameters).

DOI: 10.1021/jacs.8b11015
J. Am. Chem. Soc. 2019, 141, 451−462

Optimization of the Mn(II) concentration, polarization build-up times, as well as the field position used for DNP experiments can provide increased sensitivity in ^{17}O detection.

3.4.4. On the Mechanism of Polarization Transfer to ^{17}O at Natural Abundance. Finally, we consider the route for signal enhancement of the low abundance ^{17}O isotope. It is well-accepted that there are two steps in the polarization transfer process: the first is polarization transfer from the electrons to the core or local nuclei that are directly coupled to them (through either SE or CE). The second step is a homonuclear spin diffusion process, which spreads the polarization across the sample between the coupled nuclear spins.

Due to the extremely low abundance of ^{17}O, it is unclear whether ^{17}O nuclei are directly polarized by the Mn(II) dopants (Figure S7). ^{17}O-detected DNP sweep profile could provide some insight into the polarization transfer mechanism, but these experiments are not practical at natural isotopic abundance. As for the second step, homonuclear spin diffusion is improbable due to the low abundance of ^{17}O pairs. In order to gain more insight, we have also acquired the ^{17}O MAS-DNP spectra from a ^{6}Li enriched (95%) LTO sample doped with nominally x = 0.005 Mn(II) (Figure 10) and compared it with

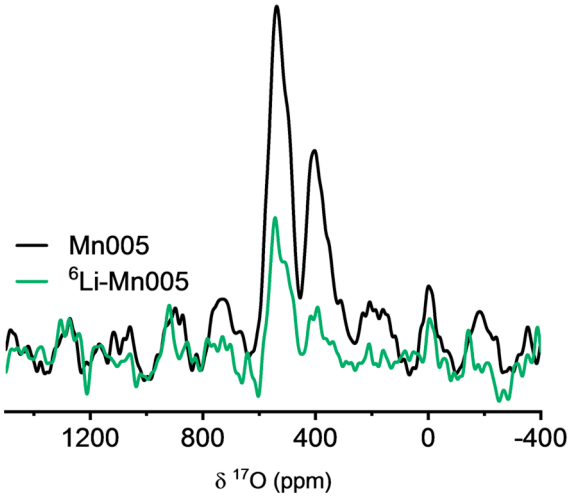

Figure 10. Comparison of ^{17}O MAS-DNP spectrum of Mn005 sample at natural abundance and with 95% ^{6}Li enrichment. Spectra were acquired with a build-up time of 170 s and 64 scans.

the nonenriched sample, while verifying that no structural change occurred compared to the nonenriched phase (Figure S22). This resulted in considerably lower ^{17}O signal intensity compared to the natural abundance sample which has 93% ^{7}Li nuclei. This result may suggest that the highly abundant nuclei (^{7}Li in the case of LTO) may play a significant role in the signal enhancement obtained for low abundance and low sensitivity nuclei. However, we note that the difference in intensity could also be the result of a longer build-up time of the ^{6}Li-enriched sample (both were acquired with a build-up time of 170 s) or the presence of a larger bath of spins which are effectively polarized in the ^{6}Li enriched sample (since the Larmor frequencies of ^{6}Li and ^{17}O are separated by only 4 MHz). The effect of the larger spin bath is also evidenced by the lower enhancement obtained for ^{6}Li in the ^{6}Li enriched sample (Figure S23). Further investigation of these two polarization transfer stages will be the subject of future studies.

4. CONCLUSIONS

We showed that Mn(II) doping provides an efficient route for sensitivity enhancement in MAS-DNP of micron sized inorganic powders. Signal enhancement factors of 142 and 24 were obtained for ^{6}Li and ^{7}Li, respectively, in LTO which translate to 4 and 2 orders of magnitude reduction in experiment time, respectively. Furthermore, DNP from Mn(II) dopants enables the detection of ^{17}O NMR spectra at natural abundance from four oxide phases, an otherwise impractical and often impossible feat for ssNMR.

The enhancement obtained in ^{6,7}Li spectra depends strongly on the concentration of the dopants. At low concentrations (here below x = 0.005 Mn(II) in LTO, which corresponds to 38 mM), we achieved close to uniform enhancement across the sample (i.e., all sites have similar enhancement factors) with minimal signal loss due to quenching effects. Higher concentrations result in distribution of enhancement factors which may be useful for elucidating the structural effects of dopants on the lattice. However, at higher concentrations the sensitivity gains decrease due to the overall lower enhancement as well as significant signal loss.

MAS-DNP via paramagnetic metal ion dopants is expected to be beneficial for elucidating the debated structural transformations occurring in LTO anode material upon electrochemical cycling. Structural insight obtained from ^{17}O DNP-NMR can also advance the development of titanate oxides as viable anode materials for Na-ion batteries. On the broader scope, this approach paves the way for sensitive structural characterization of informative nuclei, which are otherwise invisible due to the combination of low gyromagnetic ratio and isotope abundance.

■ ASSOCIATED CONTENT

Supporting Information

The Supporting Information is available free of charge on the ACS Publications website at DOI: 10.1021/jacs.8b11015.

EPR spectra of the Mn-doped phases, additional NMR and MAS-DNP data including relaxation and build-up times for ^{6,7}Li, characterization of the Li_2TiO_3 impurity phase and additional ^{17}O spectra, details on the EXAFS characterization, calculations of the probability of Li and O environments surrounding Mn(II) dopants, details on the DFT calculations including definitions, the calculated electronic structure of LTO and histograms of the calculated chemical shift and quadrupole coupling constants, and powder XRD patterns for the various oxides (PDF)

■ AUTHOR INFORMATION

Corresponding Author

*michal.leskes@weizmann.ac.il

ORCID

Anatoly I. Frenkel: 0000-0002-5451-1207
Dan Thomas Major: 0000-0002-9231-0676
Michal Leskes: 0000-0002-7172-9689

Notes

The authors declare no competing financial interest.

■ ACKNOWLEDGMENTS

We thank Dr. Raanan Carmieli for help with the CW-EPR experiments. We are grateful to Dr. Ilia Kaminker for helpful

DOI: 10.1021/jacs.8b11015
J. Am. Chem. Soc. 2019, 141, 451−462

suggestions and comments on the experiments, Prof. Shimon Vega for careful reading of the manuscript, and Shai Barlev for assistance with combinatorial calculations. We thank Prof. Daniella Goldfarb and Dr. Akiva Feintuch for acquiring the W band EPR spectra and Dr. Sabine Akabayov for help with fitting protocols of the relaxation data. This research was funded by the Planning & Budgeting Committee of the Council of High Education and the Prime Minister office of Israel, in the framework of the INREP project (M.L., D.T.M.), and the Israel Science Foundation (Grant No. 085170, M.L.) as well as support from a research grant from the Comisaroff Family Trust and Monroe and Marjorie Burk Fund for Alternative Energy Studies and the Merle S. Cahn Foundation (M.L.). H.S. and A.I.F. acknowledge support by NSF Grant No. DMR-1701747. This research used 8-ID (ISS) beamline of the National Synchrotron Light Source, a U.S. Department of Energy (DOE) Office of Science User Facility operated for the DOE Office of Science by Brookhaven National Laboratory under Contract No. DE-AC02-98CH10886. We also acknowledge the support of the BL2-2 beamline of the SSRL through the Synchrotron Catalysis Consortium (U.S. Department of Energy, Office of Basic Energy Sciences, Grant No. DE-SC0012335). Additionally, we thank Klaus Attenkofer and Janis Timoshenko for their help with EXAFS measurements at the NSLS-II and SSRL, respectively. The work was made possible in part by the historic generosity of the Harold Perlman family.

REFERENCES

(1) MacKenzie, K. J. D.; Smith, M. E. Multinuclear Solid State Nuclear Manetic Resonance of Inorganic Materials. *Pergamon Mater. Ser.* **2002**, *6*, 80001.

(2) Laws, D. D.; Bitter, H.-M. L.; Jerschow, A. Solid-State NMR Spectroscopic Methods in Chemistry. *Angew. Chem., Int. Ed.* **2002**, *41* (17), 3096−3129.

(3) Grey, C. P.; Tycko, R. Solid-State NMR in Biological and Materials Physics. *Phys. Today* **2009**, *62* (9), 44−49.

(4) Ni, Q. Z.; Daviso, E.; Can, T. V.; Markhasin, E.; Jawla, S. K.; Swager, T. M.; Temkin, R. J.; Herzfeld, J.; Griffin, R. G. High Frequency Dynamic Nuclear Polarization. *Acc. Chem. Res.* **2013**, *46* (9), 1933−1941.

(5) Maly, T.; Debelouchina, G. T.; Bajaj, V. S.; Hu, K.-N.; Joo, C.-G.; Mak-Jurkauskas, M. L.; Sirigiri, J. R.; van der Wel, P. C. A.; Herzfeld, J.; Temkin, R.; Griffin, R. G. Dynamic Nuclear Polarization at High Magnetic Fields. *J. Chem. Phys.* **2008**, *128* (5), 052211.

(6) Rossini, A. J.; Zagdoun, A.; Lelli, M.; Lesage, A.; Copéret, C.; Emsley, L. Dynamic Nuclear Polarization Surface Enhanced NMR Spectroscopy. *Acc. Chem. Res.* **2013**, *46* (9), 1942−1951.

(7) Lilly Thankamony, A. S.; Wittmann, J. J.; Kaushik, M.; Corzilius, B. Dynamic Nuclear Polarization for Sensitivity Enhancement in Modern Solid-State NMR. *Prog. Nucl. Magn. Reson. Spectrosc.* **2017**, *102−103*, 120−195.

(8) Kobayashi, T.; Perras, F. A.; Slowing, I. I.; Sadow, A. D.; Pruski, M. Dynamic Nuclear Polarization Solid-State NMR in Heterogeneous Catalysis Research. *ACS Catal.* **2015**, *5* (12), 7055−7062.

(9) Harris, J. W.; Liao, W. C.; Di Iorio, J. R.; Henry, A. M.; Ong, T. C.; Comas-Vives, A.; Copéret, C.; Gounder, R. Molecular Structure and Confining Environment of Sn Sites in Single-Site Chabazite Zeolites. *Chem. Mater.* **2017**, *29* (20), 8824−8837.

(10) Perras, F. A.; Kobayashi, T.; Pruski, M. Natural Abundance ^{17}O DNP Two-Dimensional and Surface-Enhanced NMR Spectroscopy. *J. Am. Chem. Soc.* **2015**, *137* (26), 8336−8339.

(11) Lilly Thankamony, A. S.; Lion, C.; Pourpoint, F.; Singh, B.; Perez Linde, A. J.; Carnevale, D.; Bodenhausen, G.; Vezin, H.; Lafon, O.; Polshettiwar, V. Insights into the Catalytic Activity of Nitridated Fibrous Silica (KCC-1) Nanocatalysts from ^{15}N and ^{29}Si NMR Spectroscopy Enhanced by Dynamic Nuclear Polarization. *Angew. Chem., Int. Ed.* **2015**, *54* (7), 2190−2193.

(12) Lee, D.; Takahashi, H.; Thankamony, A. S. L.; Dacquin, J.-P.; Bardet, M.; Lafon, O.; De Paëpe, G. Enhanced Solid-State NMR Correlation Spectroscopy of Quadrupolar Nuclei Using Dynamic Nuclear Polarization. *J. Am. Chem. Soc.* **2012**, *134* (45), 18491−18494.

(13) Vitzthum, V.; Miéville, P.; Carnevale, D.; Caporini, M. A.; Gajan, D.; Copéret, C.; Lelli, M.; Zagdoun, A.; Rossini, A. J.; Lesage, A.; Emsley, L.; Bodenhausen, G. Dynamic Nuclear Polarization of Quadrupolar Nuclei Using Cross Polarization from Protons: Surface-Enhanced Aluminium-27 NMR. *Chem. Commun.* **2012**, *48* (14), 1988−1990.

(14) Lesage, A.; Lelli, M.; Gajan, D.; Caporini, M. A.; Vitzthum, V.; Miéville, P.; Alauzun, J.; Roussey, A.; Thieuleux, C.; Mehdi, A.; Bodenhausen, G.; Coperet, C.; Emsley, L. Surface Enhanced NMR Spectroscopy by Dynamic Nuclear Polarization. *J. Am. Chem. Soc.* **2010**, *132* (44), 15459−15461.

(15) Hope, M. A.; Halat, D. M.; Magusin, P. C. M. M.; Paul, S.; Peng, L.; Grey, C. P. Surface-Selective Direct ^{17}O DNP NMR of CeO_2 Nanoparticles. *Chem. Commun.* **2017**, *53* (13), 2142−2145.

(16) Protesescu, L.; Rossini, A. J.; Kriegner, D.; Valla, M.; de Kergommeaux, A.; Walter, M.; Kravchyk, K. V.; Nachtegaal, M.; Stangl, J.; Malaman, B.; Reiss, P.; Lesage, A.; Emsley, L.; Coperet, C.; Kovalenko, M. V. Unraveling the Core-Shell Structure of Ligand-Capped Sn/SnO_x Nanoparticles by Surface-Enhanced Nuclear Magnetic Resonance, Mössbauer, and X-Ray Absorption Spectroscopies. *ACS Nano* **2014**, *8* (3), 2639−2648.

(17) Akbey, Ü.; Altin, B.; Linden, A.; Özçelik, S.; Gradzielski, M.; Oschkinat, H. Dynamic Nuclear Polarization of Spherical Nanoparticles. *Phys. Chem. Chem. Phys.* **2013**, *15* (47), 20706−20716.

(18) Leskes, M.; Kim, G.; Liu, T.; Michan, A. L. A. L.; Aussenac, F.; Dorffer, P.; Paul, S.; Grey, C. P. C. P. Surface-Sensitive NMR Detection of the Solid Electrolyte Interphase Layer on Reduced Graphene Oxide. *J. Phys. Chem. Lett.* **2017**, *8* (5), 1078−1085.

(19) Jin, Y.; Kneusels, N.-J. J. H.; Magusin, P. C. M. M. M. M.; Kim, G.; Castillo-Martínez, E.; Marbella, L. E.; Kerber, R. N.; Howe, D. J.; Paul, S.; Liu, T.; Grey, C. P. Identifying the Structural Basis for the Increased Stability of the Solid Electrolyte Interphase Formed on Silicon with the Additive Fluoroethylene Carbonate. *J. Am. Chem. Soc.* **2017**, *139* (42), 14992−15004.

(20) Ashbrook, S. E.; Smith, M. E. Solid State ^{17}O NMR-an Introduction to the Background Principles and Applications to Inorganic Materials. *Chem. Soc. Rev.* **2006**, *35* (8), 718−735.

(21) Wu, G. Solid-State ^{17}O NMR Studies of Organic and Biological Molecules. *Prog. Nucl. Magn. Reson. Spectrosc.* **2008**, *52* (2−3), 118−169.

(22) Perras, F. A.; Boteju, K. C.; Slowing, I. I.; Sadow, A. D.; Pruski, M. Direct ^{17}O Dynamic Nuclear Polarization of Single-Site Heterogeneous Catalysts. *Chem. Commun.* **2018**, *54* (28), 3472−3475.

(23) Blanc, F.; Sperrin, L.; Jefferson, D. A.; Pawsey, S.; Rosay, M.; Grey, C. P. Dynamic Nuclear Polarization Enhanced Natural Abundance ^{17}O Spectroscopy. *J. Am. Chem. Soc.* **2013**, *135* (8), 2975−2978.

(24) Björgvinsdóttir, S.; Walder, B. J.; Pinon, A. C.; Emsley, L. Bulk Nuclear Hyperpolarization of Inorganic Solids by Relay from the Surface. *J. Am. Chem. Soc.* **2018**, *140* (25), 7946−7951.

(25) Wenk, P.; Kaushik, M.; Richter, D.; Vogel, M.; Suess, B.; Corzilius, B. Dynamic Nuclear Polarization of Nucleic Acid with Endogenously Bound Manganese. *J. Biomol. NMR* **2015**, *63* (1), 97−109.

(26) Corzilius, B.; Michaelis, V. K.; Penzel, S. a; Ravera, E.; Smith, A. a; Luchinat, C.; Griffin, R. G. Dynamic Nuclear Polarization of ^{1}H, ^{13}C, and ^{59}Co in a Tris(Ethylenediamine)Cobalt(III) Crystalline Lattice Doped with Cr(III). *J. Am. Chem. Soc.* **2014**, *136* (33), 11716−11727.

DOI: 10.1021/jacs.8b11015
J. Am. Chem. Soc. 2019, 141, 451−462

(27) Abraham, M.; McCausland, M. A. H.; Robinson, F. N. H. Dynamic Nuclear Polarization. *Phys. Rev. Lett.* **1959**, *2* (11), 449−451.
(28) Derighetti, B.; Hafner, S.; Marxer, H.; Rager, H. NMR of ^{29}Si and ^{25}Mg In Mg_2SiO_4 with Dynamic Polarization Technique. *Phys. Lett. A* **1978**, *66* (2), 150−152.
(29) Spence, R. D.; Cowen, J. A. Concentration Dependence of the Polarization and Relaxation Time of Al27 Nuclei in Ruby. *J. Chem. Phys.* **1960**, *32* (2), 624−625.
(30) Jacquinot, J.; Wenckebach, W. T.; Goldman, M.; Abragam, A. Polarization and NMR Observation of ^{43}Ca Nuclei in CaF_2. *Phys. Rev. Lett.* **1974**, *32* (20), 1096−1097.
(31) Brun, E.; Derighetti, B.; Hundt, E. E.; Niebuhr, H. H. NMR of ^{17}O in Ruby with Dynamic Polarization Techniques. *Phys. Lett. A* **1970**, *31* (8), 416−417.
(32) Martens, R.; Müller-Warmuth, W. Structural Groups and Their Mixing in Borosilicate Glasses of Various Compositions − an NMR Study. *J. Non-Cryst. Solids* **2000**, *265* (1−2), 167−175.
(33) Chakrabarty, T.; Goldin, N.; Feintuch, A.; Houben, L.; Leskes, M. Paramagnetic Metal-Ion Dopants as Polarization Agents for Dynamic Nuclear Polarization NMR Spectroscopy in Inorganic Solids. *ChemPhysChem* **2018**, *19* (17), 2139−2142.
(34) Ohzuku, T.; Ueda, A.; Yamamoto, N. Zero-Strain Insertion Material of Li [$Li_{1/3}Ti_{5/3}$]O_4 for Rechargeable Lithium Cells. *J. Electrochem. Soc.* **1995**, *142* (5), 1431−1435.
(35) Chen, S.; Xin, Y.; Zhou, Y.; Ma, Y.; Zhou, H.; Qi, L. Self-Supported $Li_4Ti_5O_{12}$ Nanosheet Arrays for Lithium Ion Batteries with Excellent Rate Capability and Ultralong Cycle Life. *Energy Environ. Sci.* **2014**, *7* (6), 1924−1930.
(36) Yi, T.-F.; Yang, S.-Y.; Xie, Y. Recent Advances of $Li_4Ti_5O_{12}$ as a Promising next Generation Anode Material for High Power Lithium-Ion Batteries. *J. Mater. Chem. A* **2015**, *3* (11), 5750−5777.
(37) Kavan, L.; Grätzel, M. Facile Synthesis of Nanocrystalline $Li_4Ti_5O_{12}$ (Spinel) Exhibiting Fast Li Insertion. *Electrochem. Solid-State Lett.* **2002**, *5* (2), A39−A42.
(38) Zaghib, K.; Simoneau, M.; Armand, M.; Gauthier, M. Electrochemical Study of $Li_4Ti_5O_{12}$ as Negative Electrode for Li-Ion Polymer Rechargeable Batteries. *J. Power Sources* **1999**, *81*−*82*, 300−305.
(39) Thackeray, M. M. Structural Considerations of Layered and Spinel Lithiated Oxides for Lithium Ion Batteries. *J. Electrochem. Soc.* **1995**, *142* (8), 2558−2563.
(40) Ferg, E.; Gummow, R. J.; de Kock, A.; Thackeray, M. M. Spinel Anodes for Lithium-Ion Batteries. *J. Electrochem. Soc.* **1994**, *141* (11), L147−L150.
(41) Chen, C. H.; Vaughey, J. T.; Jansen, A. N.; Dees, D. W.; Kahaian, A. J.; Goacher, T.; Thackeray, M. M. Studies of Mg-Substituted $Li_{4-x}Mg_xTi_5O_{12}$ Spinel Electrodes ($0 \leq x \leq 1$) for Lithium Batteries. *J. Electrochem. Soc.* **2001**, *148* (1), A102−A104.
(42) Kaftelen, H.; Tuncer, M.; Tu, S.; Repp, S.; Göçmez, H.; Thomann, R.; Weber, S.; Erdem, E. Mn-Substituted Spinel $Li_4Ti_5O_{12}$ Materials Studied by Multifrequency EPR Spectroscopy. *J. Mater. Chem. A* **2013**, *1* (34), 9973.
(43) Su, B.; Geun, O.; Cheon, J.; Woo, J.; Jin, S.; Ho, J.; Lee, J. Photoluminescence Properties of Non-Rare Earth $MgAl_2O_4$:Mn^{2+} Green Phosphor for LEDs. *J. Ceram. Process. Res.* **2016**, *17* (7), 778−781.
(44) Shi, L.; Huang, Y.; Seo, H. J. Emission Red Shift and Unusual Band Narrowing of Mn^{2+} in $NaCaPO_4$ Phosphor. *J. Phys. Chem. A* **2010**, *114* (26), 6927−6934.
(45) Massiot, D.; Fayon, F.; Capron, M.; King, I.; Le Calve, S.; Alonso, B.; Durand, J.-O.; Bujoli, B.; Gan, Z.; Hoatson, G. Modelling One- and Two-Dimensional Solid-State NMR Spectra. *Magn. Reson. Chem.* **2002**, *40* (1), 70−76.
(46) Leskes, M.; Moore, A. J.; Goward, G. R.; Grey, C. P. Monitoring the Electrochemical Processes in the Lithium−Air Battery by Solid State NMR Spectroscopy. *J. Phys. Chem. C* **2013**, *117* (51), 26929−26939.
(47) Stoll, S.; Schweiger, A. EasySpin, a Comprehensive Software Package for Spectral Simulation and Analysis in EPR. *J. Magn. Reson.* **2006**, *178* (1), 42−55.
(48) Kresse, G.; Furthmüller, J. Efficiency of Ab-Initio Total Energy Calculations for Metals and Semiconductors Using a Plane-Wave Basis Set. *Comput. Mater. Sci.* **1996**, *6* (1), 15−50.
(49) Kresse, G.; Hafner, J. Ab Initiomolecular Dynamics for Liquid Metals. *Phys. Rev. B: Condens. Matter Mater. Phys.* **1993**, *47* (1), 558−561.
(50) Kresse, G.; Hafner, J. Ab Initio Molecular-Dynamics Simulation of the Liquid-Metal−amorphous-Semiconductor Transition in Germanium. *Phys. Rev. B: Condens. Matter Mater. Phys.* **1994**, *49* (20), 14251−14269.
(51) Laskowski, R.; Blaha, P. Calculations of NMR Chemical Shifts with APW-Based Methods. *Phys. Rev. B: Condens. Matter Mater. Phys.* **2012**, *85* (3), 035132 DOI: 10.1103/PhysRevB.85.035132.
(52) Schwarz, K.; Blaha, P. Solid State Calculations Using WIEN2k. *Comput. Mater. Sci.* **2003**, *28*, 259−273.
(53) Perdew, J.; Burke, K.; Ernzerhof, M. Generalized Gradient Approximation Made Simple. *Phys. Rev. Lett.* **1996**, *77* (18), 3865−3868.
(54) Blöchl, P. E. Projector Augmented-Wave Method. *Phys. Rev. B: Condens. Matter Mater. Phys.* **1994**, *50* (24), 17953−17979.
(55) Monkhorst, H.; Pack, J. Special Points for Brillouin Zone Integrations. *Phys. Rev. B* **1976**, *13* (12), 5188−5192.
(56) Feynman, R. P. Forces in Molecules. *Phys. Rev.* **1939**, *56* (4), 340−343.
(57) Ravel, B.; Newville, M. ATHENA, ARTEMIS, HEPHAESTUS: Data Analysis for X-Ray Absorption Spectroscopy Using IFEFFIT. *J. Synchrotron Radiat.* **2005**, *12* (4), 537−541.
(58) Kaushik, M.; Bahrenberg, T.; Can, T. V.; Caporini, M. A.; Silvers, R.; Heiliger, J.; Smith, A. A.; Schwalbe, H.; Griffin, R. G.; Corzilius, B. Gd(III) and Mn(II) Complexes for Dynamic Nuclear Polarization: Small Molecular Chelate Polarizing Agents and Applications with Site-Directed Spin Labeling of Proteins. *Phys. Chem. Chem. Phys.* **2016**, *18* (39), 27205−27218.
(59) Shimon, D.; Hovav, Y.; Feintuch, A.; Goldfarb, D.; Vega, S. Dynamic Nuclear Polarization in the Solid State: A Transition between the Cross Effect and the Solid Effect. *Phys. Chem. Chem. Phys.* **2012**, *14* (16), 5729−5743.
(60) Takahashi, H.; Lee, D.; Dubois, L.; Bardet, M.; Hediger, S.; De Paëpe, G. Rapid Natural-Abundance 2D ^{13}C-^{13}C Correlation Spectroscopy Using Dynamic Nuclear Polarization Enhanced Solid-State NMR and Matrix-Free Sample Preparation. *Angew. Chem., Int. Ed.* **2012**, *51* (47), 11766−11769.
(61) Perras, F. A.; Wang, L.-L. L.; Manzano, J. S.; Chaudhary, U.; Opembe, N. N.; Johnson, D. D.; Slowing, I. I.; Pruski, M. Optimal Sample Formulations for DNP SENS: The Importance of Radical-Surface Interactions. *Curr. Opin. Colloid Interface Sci.* **2018**, *33*, 9−18.
(62) Lee, D.; Hediger, S.; De Paëpe, G. Is Solid-State NMR Enhanced by Dynamic Nuclear Polarization? *Solid State Nucl. Magn. Reson.* **2015**, *66*−*67*, 6−20.
(63) Rossini, A. J.; Zagdoun, A.; Lelli, M.; Gajan, D.; Rascón, F.; Rosay, M.; Maas, W. E.; Copéret, C.; Lesage, A.; Emsley, L. One Hundred Fold Overall Sensitivity Enhancements for Silicon-29 NMR Spectroscopy of Surfaces by Dynamic Nuclear Polarization with CPMG Acquisition. *Chem. Sci.* **2012**, *3* (1), 108−115.
(64) Mentink-Vigier, F.; Paul, S.; Lee, D.; Feintuch, A.; Hediger, S.; Vega, S.; De Paëpe, G. Nuclear Depolarization and Absolute Sensitivity in Magic-Angle Spinning Cross Effect Dynamic Nuclear Polarization. *Phys. Chem. Chem. Phys.* **2015**, *17* (34), 21824−21836.
(65) Corzilius, B.; Andreas, L. B.; Smith, A. a; Ni, Q. Z.; Griffin, R. G. Paramagnet Induced Signal Quenching in MAS-DNP Experiments in Frozen Homogeneous Solutions. *J. Magn. Reson.* **2014**, *240*, 113−123.
(66) Kataoka, K.; Takahashi, Y.; Kijima, N.; Akimoto, J.; Ohshima, K.-i. Single Crystal Growth and Structure Refinement of $Li_4Ti_5O_{12}$. *J. Phys. Chem. Solids* **2008**, *69* (5−6), 1454−1456.

DOI: 10.1021/jacs.8b11015
J. Am. Chem. Soc. 2019, 141, 451−462

(67) Xu, Z.; Stebbins, J. F. ^{6}Li Nuclear Magnetic Resonance Chemical Shifts, Coordination Number and Relaxation in Crystalline and Glassy Silicates. *Solid State Nucl. Magn. Reson.* **1995**, *5* (1), 103−112.
(68) Grey, C. P.; Dupré, N. NMR Studies of Cathode Materials for Lithium-Ion Rechargeable Batteries. *Chem. Rev.* **2004**, *104* (10), 4493−4512.
(69) Schmidt, W.; Wilkening, M. Discriminating the Mobile Ions from the Immobile Ones in $Li_{4+x}Ti_5O_{12}$:^{6}Li NMR Reveals the Main Li + Diffusion Pathway and Proposes a Refined Lithiation Mechanism. *J. Phys. Chem. C* **2016**, *120* (21), 11372−11381.
(70) Pigliapochi, R.; Seymour, I. D.; Merlet, C.; Pell, A. J.; Murphy, D. T.; Schmid, S.; Grey, C. P. Structural Characterization of the Li-Ion Battery Cathode Materials $LiTi_xMn_{2-x}O_4$ ($0.2 \leq x \leq 1.5$): A Combined Experimental ^{7}Li NMR and First-Principles Study. *Chem. Mater.* **2018**, *30* (3), 817−829.
(71) Vijayakumar, M.; Kerisit, S.; Yang, Z.; Graff, G. L.; Liu, J.; Sears, J. a; Burton, S. D.; Rosso, K. M.; Hu, J. Combined ^{6,7}Li NMR and Molecular Dynamics Study of Li Diffusion in Li 2 TiO 3. *J. Phys. Chem. C* **2009**, *113* (46), 20108−20116.
(72) Tsai, P. -c.; Hsu, W.-D.; Lin, S. -k. Atomistic Structure and Ab Initio Electrochemical Properties of $Li_4Ti_5O_{12}$ Defect Spinel for Li Ion Batteries. *J. Electrochem. Soc.* **2014**, *161* (3), A439−A444.
(73) Pickard, C. J.; Mauri, F. All-Electron Magnetic Response with Pseudopotentials: NMR Chemical Shifts. *Phys. Rev. B: Condens. Matter Mater. Phys.* **2001**, *63* (24), 1−13.
(74) Yates, J. R.; Pickard, C. J.; Mauri, F. Calculation of NMR Chemical Shifts for Extended Systems Using Ultrasoft Pseudopotentials. *Phys. Phys. Rev. B: Condens. Matter Mater. Phys.* **2007**, *76* (2), 24401−24412.
(75) Bastow, T. J.; Dirken, P. J.; Smith, M. E.; Whitfield, H. J. Factors Controlling the ^{17}O NMR Chemical Shift in Ionic Mixed Metal Oxides. *J. Phys. Chem.* **1996**, *100* (47), 18539−18545.
(76) Hernandez, V. S.; Martinez, L. M. T.; Mather, G. C.; West, A. R. Stoichiometry, Structures and Polymorphism of Spinel Like Phases, $Li_{1.33x}Zn_{2-2x}Ti_{1+0.67x}O_4$. *J. Mater. Chem.* **1996**, *6* (9), 1533−1536.
(77) Sickafus, K. E. Radiation Tolerance of Complex Oxides. *Science* **2000**, *289* (5480), 748−751.
(78) Maekawa, H.; et al. Cation Mixing in Natural $MgAl_2O_4$ Spinel: A High-Temperature ^{27}Al NMR Study. *Am. Mineral.* **1997**, *82*, 1125−1132.
(79) Millard, R. L.; Peterson, R. C.; Hunter, B. K. Temperature Dependence of Cation Disorder in $MgAl_2O_4$ Spinel Using ^{27}Al and ^{17}O Magic-Angle Spinning NMR. *Am. Mineral.* **1992**, *77* (1−2), 44−52.

DOI: 10.1021/jacs.8b11015
J. Am. Chem. Soc. 2019, 141, 451−462